Atomic scale synergistic interactions lead to breakthrough catalysts for electrocatalytic water splitting

Chun-Lung Huang [a], Yan-Gu Lin [b], Chao-Lung Chiang [b], Chun-Kuo Peng [b,c], Duraisamy Senthil Raja [a], Cheng-Ting Hsieh [a], Yu-An Chen [a], Shun-Qin Chang [a], Yong-Xian Yeh [a], Shih-Yuan Lu [a,*]

[a] Department of Chemical Engineering, National Tsing Hua University, Hsinchu 30013, Taiwan ROC
[b] National Synchrotron Radiation Research Center, Hsinchu 30076, Taiwan ROC
[c] Department of Materials Science and Engineering, National Yang Ming Chiao Tung University, Hsinchu 30010, Taiwan ROC

ARTICLE INFO

ABSTRACT

A breakthrough catalyst for electrocatalytic water splitting, precious-metal-free equi-molar high entropy alloy H-FeCoNiCuMo, is developed through exploring and maximizing strong synergistic interactions between atomically well-mixed constituents of H-FeCoNiCuMo over atomic scales. For overall electrolytic water splitting under severe industrial operation conditions, the H-FeCoNiCuMo//H-FeCoNiCuMo couple requires only an ultralow cell voltage of 1.627 V to deliver an ultrahigh current density of 1500 mA cm^{-2}, and remains stable after a 100-hr continuous operation, largely outperforming a precious metal-based benchmark couple, Pt/C//IrO$_2$, 2.038 V with 55% decay in 24 hr. A new catalytic phenomenon is discovered, two different catalytic mechanisms functioning simultaneously on different constituents of H-FeCoNiCuMo, the Volmer-Heyrovsky route on Co and Cu and Volmer-Tafel route on Ni and Mo, from which a new kinetic model is formulated to predict a new theoretical lower limit of Tafel slope of 15 mV dec^{-1} for hydrogen evolution reactions.

1. Introduction

Deep decarbonization is the sole remedy to realize the two-degree-scenario (2DS) set by the Paris Climate Agreement and hydrogen plays a key role. Some expect decarbonization through hydrogen economy to fill half gap of the carbon dioxide emission reduction required towards 2DS [1]. The core of the hydrogen economy is green hydrogen production. Unfortunately, up to the present, fossil fuels-based hydrogen generation, such as steam-methane reforming, which produces comparable amounts of CO$_2$ as the by-product, still dominates [2]. On the other hand, hydrogen production through renewable energy driven electrolytic water splitting is a green process, which is environmental unfriendly and sustainable. To reach the goal of net-zero CO$_2$ emission by 2050, renewable energy driven electrolytic water splitting must prevail as a major hydrogen generation technology. Furthermore, this technology also serves as a necessary energy storage route to resolve the intolerable intermittency and unreliability issues of renewable energies. The prevailing of this hydrogen production technology however is restricted by the high cost of electricity. Consequently, developments of

cost-effective highly efficient and stable electrocatalysts to drive the electrolytic water splitting reactions are the key. Traditional Earth-scarce precious metal based electrocatalysts, such as Pt/C, IrO$_2$, and RuO$_2$, although highly efficient, are not applicable for large scale hydrogen production, and the development of precious metal free electrocatalysts of cost-effectiveness, high efficiency, and high stability is most critical.

In terms of catalyst developments, mono-component systems are first explored, followed by multi-component systems, taking advantages of possible positive synergy between constituent components [3–9]. Recently, a new class of multi-component catalyst systems, entropy-stabilized materials, including alloys, oxides, sulfides, phosphides, etc. [10–12], emerges and is demonstrated superior bifunctional features toward water splitting reactions. In light of the variable and flexible element compositions, entropy-stabilized materials provide infinite and enormous potentials for the design of promising electrocatalysts. The key is to maximize the synergy between constituent components. With an assumption of equally active components, the interaction between constituents of a multi-component system is

maximum if the constituents are most randomly distributed in the system. And the maximum extent of randomness of a multi-component system can be achieved if the configurational entropy of the system is maximized. Considering a system composed of N components, its molar configurational entropy (S_{config}) can be expressed as $-R\sum_{i=1}^{N}x_i ln(x_i)$. Here, R is the universal gas constant and x_i is the molar fraction of component i. The maximum of S_{config} can be derived, by requiring $\partial S_{\text{config}}/\partial x_i = 0$ and $\partial^2 S_{\text{config}}/\partial x_i^2 < 0$ subject to the constraint $\sum_{i=1}^{N}x_i = 1$, to be obtained at $x_i = 1/N$, i.e., equi-molar constituents in the catalyst, and the maximum is equal to $R\,ln\,(N)$, a monotonically increasing function of N. Ideally, increasing composition complexity of the multi-component system increases the total synergistic effects between constituent components, provided that the constituents are atomically/molecularly well-mixed and possess positive inter-atomic/molecular synergistic effects. For heterogeneous reactions, catalyzation occurs on the surface of the catalyst. Atomically/molecularly well-mixed equi-molar multi-component catalysts possess maximal synergistic effects not only in the bulk but also on the surface to function for heterogeneous reactions. It is to be cautioned that the present work focuses on exploration of synergistic effects between constituent components on catalytic efficiency. Nevertheless, the catalytic efficiency of a catalyst may also well be influenced by many other factors, such as specific facet exposure, defect concentrations, phase segregation, etc. With the above consideration in mind, we design an atomically well-mixed multi-component alloy as the candidate catalyst for electrolytic water splitting. First, precious metals are excluded from the consideration to ensure applicability in large scale production and only relatively Earth-abundant transition metals are considered. Second, Ni, Mo, and Cu are included since it has been demonstrated that NiMo and NiCu alloys are excellent catalysts for catalyzation of hydrogen evolution reactions (HER) at cathodes [13,14]. Third, Fe and Co, in addition to Ni, are also included since Fe, Co, and Ni based materials are popular and excellent catalysts for catalyzation of oxygen evolution reactions (OER) at anodes, with the corresponding oxyhydroxides formed in-situ during the OER serving as the active species [15–19]. Fourth, taking the clue from the maximum configurational entropy approach, the five chosen metallic elements are to be atomically well-mixed at relatively equi-molar in the alloy. The targeted catalyst is thus precious-metal-free high entropy alloys (HEA) composed of Fe, Co, Ni, Cu, and Mo.

High entropy alloys, defined as alloys composed of five or more major metallic elements, have been under intensive and extensive development in past fifteen years for their extraordinary mechanical, magnetic, and corrosion properties [20,21]. The application of HEAs on electrocatalytic water splitting is however still in its infancy, with breakthroughs yet to be realized, and the merits of HEAs as water splitting electrocatalysts, even as catalysts in general, are far from being fully explored [22–25]. Herein, we synthesize an equi-molar FeCoNiCuMo HEA on nickel foam, denoted as H-FeCoNiCuMo, with a fast (50 min), simple, low temperature (50 °C), and scalable pulse current electrodeposition method. High temperature processes are often required for syntheses of HEAs because of the favorable entropic stabilization achieved at high temperatures for single phase formation. The low temperature operation of the present method warrants it highly energy-efficient for HEA production, as compared with highly energy-demanding arc melting and mechanical alloying methods [20, 26]. H-FeCoNiCuMo exhibits breakthrough electrocatalytic performances for both HER and OER, achieving single digit η_{10} for the HER in both alkaline and acidic electrolytes (7 and 9 mV in 1 M KOH and 0.5 M H$_2$SO$_4$, respectively) and ultralow, less than 200 mV η_{10} for the OER in alkaline electrolytes (194 mV in 1 M KOH), outperforming those of the popular benchmark precious metal based Pt/C (15 and 14 mV in 1 M KOH and 0.5 M H$_2$SO$_4$, respectively) for the HER and IrO$_2$ (294 mV in 1 M KOH) and RuO$_2$ (232 mV in 1 M KOH) for the OER. Here, η_x is defined as the overpotential required to achieve a current density of x

mA cm^{-2}. For overall water splitting, it requires only an ultralow cell voltage of 1.416 V to drive a current density of 10 mA cm^{-2} for the H-FeCoNiCuMo//H-FeCoNiCuMo couple, significantly lower than 1.542 and 1.472 V achieved by the Pt/C//IrO$_2$ couple and the Pt/C//RuO$_2$ couple, respectively. Note that all current density data reported herein are geometric area based.

2. Experimental section

2.1. Materials

Anhydrous iron(III) chloride (FeCl$_3$, 99%), nickel chloride hexahydrate (NiCl$_2$0.6 H$_2$O, 96%), cobalt(II) chloride hexahydrate (CoCl$_2$·6 H$_2$O, ≥97%), copper(II) chloride dihydrate (CuCl$_2$0.2 H$_2$O, 99%), and trisodium citrate dihydrate (Na$_3$C$_6$H$_5$O$_7$0.2 H$_2$O, 99%) were obtained from Showa Kako Corp. Sodium hydroxide (NaOH, 99%), potassium hydroxide (KOH, 85%), and sodium dodecyl sulfate (SDS, 98%) were purchased from Honeywell International Inc. Phosphate buffer saline solutions (PBS, 1 M, pH ~ 7.4) were obtained from Sigma-Aldrich, Inc. Ruthenium(IV) oxide (RuO$_2$, 99.5%) was purchased from ACROS Organics. Hydrochloric acid (HCl, 37%), ammonium hydroxide (NH$_4$OH, 28–30%), and sulfuric acid (H$_2$SO$_4$, 98%) were purchased from J. T. Baker. N-Methyl-2-pyrrolidone (NMP, 99.9%), iridium (IV) oxide (IrO$_2$), 20 wt% platinum on carbon black (Pt/C), iron (Fe, 99.6%), cobalt (Co, 99.8%), nickel (Ni, 99.9%), copper (Cu, 99.9%), molybdenum (Mo, 99.95%), carbon paper, and sodium molybdate dihydrate (Na$_2$MoO$_4$0.2 H$_2$O, 99%), were obtained from Alfa Aesar. Deionized water (DI water, electrical resistance ~18 MΩ) was produced with a Milli-Q® Advantage A10 system. All chemicals were used as received.

2.2. HEA and MEA electrodes

Equi-molar FeCoNiCuMo HEA with dendritic structure were deposited on nickel foam (NF), denoted as H-FeCoNiCuMo, with a pulse current (PC) electrodeposition method. First, a 1.7 mm-thick, 1 cm-long, and 0.5 cm-wide nickel foam of 100 ppi (pores per inch) was sequentially cleaned with acetone, ethanol, and DI water. A conventional three-electrode cell was used for the fabrication of the H-FeCoNiCuMo electrode. The nickel foam served as the working electrode for the electrodeposition, and a graphite rod (8 cm-long and 0.5 cm in diameter) and Ag/AgCl were used as the counter and reference electrodes, respectively. The electrolyte (25 mL) was prepared by mixing 0.2 g L^{-1} SDS, 0.25 M anhydrous FeCl$_3$, 0.3 M CoCl$_2$, 0.5 M NiCl$_2$, 4 mM CuCl$_2$, 0.045 M Na$_2$MoO$_4$, and 0.4 M Na$_3$C$_6$H$_5$O$_7$ in DI water, followed by adjusting the pH value of the electrolyte to 9 using NH$_4$OH. The electrodeposition of FeCoNiCuMo HEA was conducted at a pulse current mode at 50 °C by using an electrochemical workstation (CHI 1128 C, CH Instruments, Inc.). The pulse current density was set at $-$ 4 A cm^{-2} and operated at a duty cycle of 0.2 s (on)/0.8 s (off) for 3000 cycles. The electrolyte was stirred at 300 rpm. As for the fabrication of the control electrodes, including M-FeCoNiCu, M-FeCoNiMo, M-CoNiCuMo, M-FeNiCuMo, and M-FeCoCuMo, the procedures were the same as above, only that the electrolyte compositions were different as summarized in Table S1. FeCoNiCuMo HEA was also deposited onto nickel plates (NP) and carbon papers (CP) with the same deposition procedures and conditions as for H-FeCoNiCuMo for electrochemical characterizations.

2.3. Benchmark electrodes (RuO$_2$, IrO$_2$, and Pt/C)

Benchmark electrodes were fabricated by loading nickel foam with 2 mg cm^{-2} IrO$_2$ (RuO$_2$) and 20 wt% Pt/C powders for the OER and HER, respectively. A homogeneous ink suspension was first prepared by dispersing 8 mg of the catalyst powder in a mixture solution containing 300 μL of 50% aqueous ethanol and 100 μL of polyvinylidene fluoride, which contained 0.3 wt% PVDF as the binder in an NMP solvent, followed by ultrasonication for 30 min. One hundred μL of the ink was

spread onto a 100 ppi nickel foam by drop-casting. Subsequently, as-prepared benchmark electrodes were dried at 70 °C in a vacuum oven for 24 hr.

2.4. Mix-FeCoNiCuMo and MA-FeCoNiCuMo electrodes

High purity powders of Fe, Co, Ni, Cu, and Mo ($\geq$ 99.5 wt%) of particle sizes of 100–300 mesh were used as the starting material. The powders were mixed in equi-molar (Fe:Co:Ni:Cu:Mo = 1:1:1:1:1) and milled at 250 rpm for 36 h in a planetary ball miller (YXQM-1 L, MITR) under an argon atmosphere. Yttria-stabilized zirconia (YSZ) and stainless steel balls were used as the milling media at a ball-to-powder ratio of 15:1. After that, 0.8 g of mixed powders with or without ball milling was loaded into a stainless-steel mold and pressed at room temperature under a pressure of 600 MPa for 5 min to form a $10\times10\times1$ mm bulk electrode. Here, the bulk electrode with and without the ball milling treatment was denoted as MA-FeCoNiCuMo and Mix-FeCoNiCuMo, respectively.

2.5. Structural characterizations

The crystalline structures of HEA and MEAs were characterized with high-energy XRD conducted at Taiwan Photon Source (XRD: TPS 09 A) beamline stations of the National Synchrotron Radiation Research Center (NSRRC) of Taiwan. Appropriate amounts of HEA and MEAs powders were loaded into a capillary tube (10 mm-long and 0.5 mm in diameter with a clay-sealed end) up to a depth of 8 mm, followed by placing the tube in a Kapton sample adapter at an X-ray-center-calibrated position for the XRD characterization (λ = 0.6888 Å). The diffraction intensity and position of the sample were automatically optimized with a multi-crystal analyzer, and recorded in a desktop computer. These recorded diffraction signals were exported to raw data files, wavelength-calibrated to Cu Kα (λ = 1.5406 Å), and depicted with WinPOLTR software for further comparison with standard XRD patterns available in database.

A field emission scanning electron microscope (FESEM) (Hitachi S-8010, Hitachi High-Technologies Corp.) was used to observe the morphology of the HEA and MEAs electrodes. To acquire crystalline structure images, a high resolution transmission electron microscope (HRTEM) (JEM-F200, JEOL ltd.) was used. The samples were dispersed in an isopropanol solution and the resulting suspension was drop-casted onto a carbon coated Au grid, followed by drying in air for 30 min. Annular bright-field scanning transmission electron microscopy (ABF-STEM) and the accompanying Energy-dispersive X-ray spectroscopy (EDX) elemental mapping (X-Max N 100TLE, Oxford Instruments plc) were conducted at an accelerating voltage of 200 kV to quantify the composition of the samples. Chemical and electronic states of the constituent elements of the samples were investigated with a high-resolution X-ray photoelectron spectroscope (HRXPS) (ULVAC-PHI XPS, ULVAC-PHI Inc.) using a monochromatized Al Kα X-ray as the excitation source. The elemental compositions of HEA and MEAs were determined using an inductively coupled plasma-optical emission spectrometer (ICP-OES, Thermo Scientific iCAP 7000 Plus Series).

2.6. Phase stability in H-FeCoNiCuMo

Four parameters were used to judge the possible phase of H-FeCoNiCuMo: atomic size difference (δ), mixing enthalpy (ΔH_{mix}), mixing entropy (ΔS_{mix}), and valence electron concentration (VEC). They are defined as follows.

(1) Atomic size difference (δ):

$$\delta = \sqrt{\sum_{i=1}^{n} c_i \left(1 - \frac{r_i}{\bar{r}}\right)}$$

where $\bar{r}$ = $\sum_{i=1}^{n} c_i r_i$ is the average atomic radius, r_i the atomic radius of the ith element, and c_i the atomic percentage of the ith element.

(2) Mixing enthalpy (ΔH_{mix})

$$\Delta H_{mix} = \sum_{i=1,i\neq j}^{n} \Omega_{ij} c_i c_j$$

where Ω_{ij} = $4\Delta H_{mix}^{AB}$ is the regular solution interaction parameter between the ith and jth elements and ΔH_{mix}^{AB} is the enthalpy of mixing of binary liquid alloys.

(3) Mixing entropy (ΔS_{mix}):

$$\Delta S_{mix} = -R \sum_{i=1}^{n} c_i \ln c_i$$

where R is the gas constant.

(4) Valence electron concentration (VEC):

$$VEC = \sum_{i=1}^{n} c_i (VEC)_i$$

where $(VEC)_i$ is the VEC for the ith element.

2.7. Electrochemical characterizations for OER and HER

The OER and HER characterizations of the sample electrodes were conducted with a conventional three-electrode system on an electrochemical analysis system (CHI 6273E). The sample served as the working electrode with a graphite plate (1 cm × 1 cm in size) serving as the counter electrode. An Hg/HgO electrode (RE-61AP) or Ag/AgCl electrode was used as the reference electrode for characterizations in 1 M KOH (pH~13.8)/PBS (pH~7.4) or 0.5 M H_2SO_4 (pH~0), respectively. The working electrode was conditioned with a 60-cycle cyclic voltammetry (CV) at a scan rate of 100 mV s^{-1} to saturate the electrolyte with product gases and to stabilize the sample catalyst. For linear sweep voltammetry (LSV) characterizations in 1 M KOH, the potential windows were set at 0–1.0 V (vs. Hg/HgO) and − 0.8 to − 1.5 V (vs. Hg/HgO) for HER and OER, respectively. For those in 1 M PBS, the potential windows were set at 0–1.5 V (vs. Hg/HgO) and − 0.5 to − 1.5 V (vs. Hg/HgO) for HER and OER, respectively. As for the HER in 0.5 M H_2SO_4, the LSV curves were recorded in a potential window of − 0.2 to − 0.8 V (vs. Ag/AgCl). For all LSV characterizations, the scan rate was set at 1 mV s^{-1}. The use of the slow scan rate of 1 mV s^{-1} avoids possible interferences from capacitive currents in determination of overpotentials. All current densities reported were iR-compensated and all potential values reported were referred to the reverse hydrogen electrode (RHE). The iR-compensation was conducted based on the solution resistance detected by the CHI workstation, and overpotentials (η) were computed with η = E$_{RHE}$ - 1.23 for the OER.

Electrochemical impedance spectroscopy (EIS) was conducted in a conventional three-electrode system, with the frequency ranging from 100 mHz to 100 kHz and the potential set at a value ensuring the occurrence of the OER (0.7 V vs. Hg/HgO in 1 M KOH) and HER (−1.1 V vs. Hg/HgO in 1 M KOH and −0.5 V vs. Ag/AgCl in 0.5 M H_2SO_4). An equivalent circuit model, containing five circuit components including electrode porosity resistances, system resistances, constant phase element, charge transfer resistances, and double-layer capacitances, denoted as R_p, R_s, CPE, R_{ct}, and C_{dl}, respectively, was used to fit the EIS data, as presented in Figs. S15, S18, and S22, to study the kinetic characteristics of the system. Here, R_{ct} quantifies the charge transfer resistance at the involved Faradaic reactions (OER or HER), and is a critical parameter to assess the kinetic behavior of the system. It was determined and summarized in Tables S5, S6, and S8 for comparison.

Overall water splitting measurements were conducted in 1 M KOH

with a two-electrode system. The electrodes were first conditioned with a 60-cycle cyclic voltammetry at a scan rate of 100 mV s^{-1} over potential windows of 0–1.0 V (vs. Hg/HgO) and − 0.8 to − 1.5 V (vs. Hg/HgO) for the anode and cathode, respectively. Then, the LSV curves were recorded in the potential window of 1–2.2 V at a scan rate of 1 mV s^{-1}. The mass loading of H-FeCoNiCuMo was controlled to be around 10 mg cm^{-2}.

2.8. Determination of electrochemical active surface area (ECSA) and turnover frequency (TOF)

To estimate ECSA of the sample electrode, CV curves recorded at increasing scan rates of 20, 40, 60, 80, and 100 mV s^{-1} within a non-Faradaic potential window (0–0.1 V vs. Hg/HgO and −0.2 to −0.1 V vs. Ag/AgCl for 1 M KOH and 0.5 M H$_2$SO$_4$, respectively) (Figs. S11, and S20) were collected. The value of C_{dl} was then calculated by using the slope (=2 C_{dl}) of the current density difference (Δj) at 0.05 V (vs. Hg/HgO) and − 0.15 V (vs.Ag/AgCl) vs. scan rate plot in 1 M KOH and 0.5 M H$_2$SO$_4$, respectively (Figs. S12 and S21).

Here, we chose H-FeCoNiCuMo as a calculation example. The measured capacitive current density differences are plotted as a function of the scan rate in Fig. S12 and a linear fitting determines the slope to be 9.32 mF cm^{-2} for the H-FeCoNiCuMo. The specific capacitance can be converted into an ECSA using the specific capacitance value of a real flat surface area as a reference. For most metals, typical Helmholtz capacitances (specific capacitances) range from 20 to 60 μF cm^{-2} for a flat surface. Therefore, in the following calculations of TOF, we take 40 μF cm^{-2} (midpoint of 20–60 μF cm^{-2}) as the specific capacitance for a flat metal surface.

ECSA of H-FeCoNiCuMo.

$$A_{ECSA}^{H-FeCoNiCuMo} = \frac{4.66\ mF\ cm^{-2}}{40\ \mu F\ cm^{-2}\ per\ cm_{ECSA}^2} = 116.5$$

Calculation of turnover frequency TOF:

TOF (s^{-1}) was determined by the following equation.

$$TOF = \frac{total\ number\ of\ hydrogen\ turn\ overs * j}{total\ number\ of\ active\ sites * A_{ECSA}^{H-FeCoNiCuMo}}$$

The total number of hydrogens turnovers was calculated from the current density according to:

$$\#_{H_2}\ at\ j\quad mA\ cm^{-2} = j\frac{mA}{cm^2} * \frac{1C\ s^{-1}}{1000\ mA} * \frac{1\ mol\ e^{-1}}{96485.3\ C} * \frac{1\ mol\ H_2}{2\ mol\ e^{-}} * \frac{6.022*10^{23}\ H_2\ molecules}{1\ mol\ H_2} = 3.12*10^{15}\ \frac{H_2 s^{-1}}{cm^2} * j$$

The number of active sites of H-FeCoNiCuMo per real surface area:

From Fig. 1 C, the lattice constant of H-FeCoNiCuMo is 0.363 nm and there are 4 atoms per unit cell in an FCC phase. The number of exposed active sites of H-FeCoNiCuMo is estimated as follows:

$$\#_{active\ sites} = \left(\frac{4\ atoms\ per\ unit\ cell}{0.3637\ nm^3 per\ unit\ cell}\right)^{2/3} = 1.87 * 10^{15} atoms\ cm_{real}^{-2}$$

Then, TOF of H-FeCoNiCuMo for the HER at η$_{50}$ (j = 152.9 mA cm^{-2}) can be determined:

$$TOF_{HER} = \frac{3.12 * 10^{15}\ \frac{H_2 s^{-1}}{cm^2} * 152.9}{1.87 * 10^{15} atoms\ cm_{real}^{-2} * 116.5} = 2.19\ s^{-1}$$

For overall water splitting reaction, there is only one half O$_2$ generated. Therefore, the TOF of H-FeCoNiCuMo for the OER at η$_{300}$ (j = 816.5 mA cm^{-2}) was determined as follows:

$$TOF_{OER} = \frac{3.12*10^{15}\ \frac{H_2 s^{-1}}{cm^2} * 816.5}{2*1.87*10^{15} atoms\ cm_{real}^{-2} * 116.5} = 5.85\ s^{-1}$$

2.9. In-situ X-ray absorption and EXAFS analysis

For in-situ X-ray absorption (XAS) study of electrolytic water splitting, the intensity of the incident X-ray beam is significantly weakened by X-ray absorption of the electrolyte, allowing X-ray probing limited to the catalyst/electrolyte interface where the catalyzation occurs. The carbon cloths electrodes coated with HEA or MEA powders were used for in-situ XAS measurements (performed at TPS 44 A). The front and back hollows of a three-electrode Teflon holder were adhered to each other with two pieces of transparent Kapton tapes (5.0 ×5.0 cm^2), allowing the X-ray beam to pass through the holder. Subsequently, the carbon cloth electrode, Pt wire, and Hg/HgO or Ag/AgCl electrode were placed in the acidic or alkaline electrolyte-filled (alkaline electrolyte: 1.0 M KOH; acidic electrolyte: 0.5 M H$_2$SO$_4$) holder, and connected to a laptop-linked electrochemical workstation (CHI 6278E, CH Instrument, Inc.) with three clip-head electrode wires, to serve as the working, counter, and reference electrodes, respectively. The carbon cloth electrode was applied potentials (vs. Hg/HgO or Ag/AgCl) at specific voltages (−0.935, −1.035, −1.235, and −1.435 V in 1.0 M KOH; −0.221, −0.321, −0.521, and −0.721 V in 0.5 M H$_2$SO$_4$) and probed in-situ with an X-ray beam under a chronoamperometric mode for 5 min

Extended X-ray absorption fine structure (EXAFS) spectra were converted to be k^2-weighted in the region of 3.0–9.0 Å^{-1}, and then Fourier-transformed to FT-EXAFS spectra with phase-correction to analyze the coordination environment (i.e., coordination number, bond distance, and Debye-Waller factor) of Fe, Co, Ni, Cu, and Mo in the alloy samples for further comparisons and discussions. Five standard face-centered structure (FCC) metallic models (Fe, Co, Ni, Cu, and Mo), downloaded from the online Inorganic Crystal Structure Database (ICSD) (https://icsd.fiz-karlsruhe.de/), were used as the references for the alloy samples for model fitting of the FT-EXAFS spectra using Artemis software (version of 0.9.26).

3. Results and discussion

3.1. Catalyst characterizations

FeCoNiCuMo HEAs are deposited on skeleton surfaces of a nickel foam with a pulse current electrodeposition method using suitably formulated precursor electrolytes to fabricate H- FeCoNiCuMo electrodes (Fig. 1A, Table S1). For comparison purposes, corresponding four metallic element based medium-entropy alloy (MEA) electrodes are also fabricated (Table S1). The HEA/MEAs are nearly equi-molar in composition (Table S2), with a 3-dimensional dendritic structure, induced by the strong bubble-releasing side reaction of hydrogen evolution during alloy deposition operated at a high current density (Fig. 1B, Fig. S2) [27]. The HEA/MEA are densely populated on the skeleton surfaces of the nickel foam (Fig. 1A and 1B, Fig. S2). The FeCoNiCuMo HEA possesses a single face-centered cubic (FCC) phase, with no sign of phase separation, implying an atomically well mixed alloy (Fig. 1C, and Fig. S1). Its interplanar spacing is determined with high-resolution transmission electron microscopy (HRTEM) to be 0.21 nm for the (111) planes and 0.181 nm for the (220) planes (Fig. 1 C). The lattice constant, as estimated from Vegard's rule, is 0.366 nm, in excellent agreement with 0.364 nm from HRTEM and 0.363 nm from XRD (Fig. 1E) measurements, together with the uniform distribution of the five constituent elements (Fig. 1D; for MEAs: Figs. S3-S7), further confirming its HEA characteristics. Crystallinity of
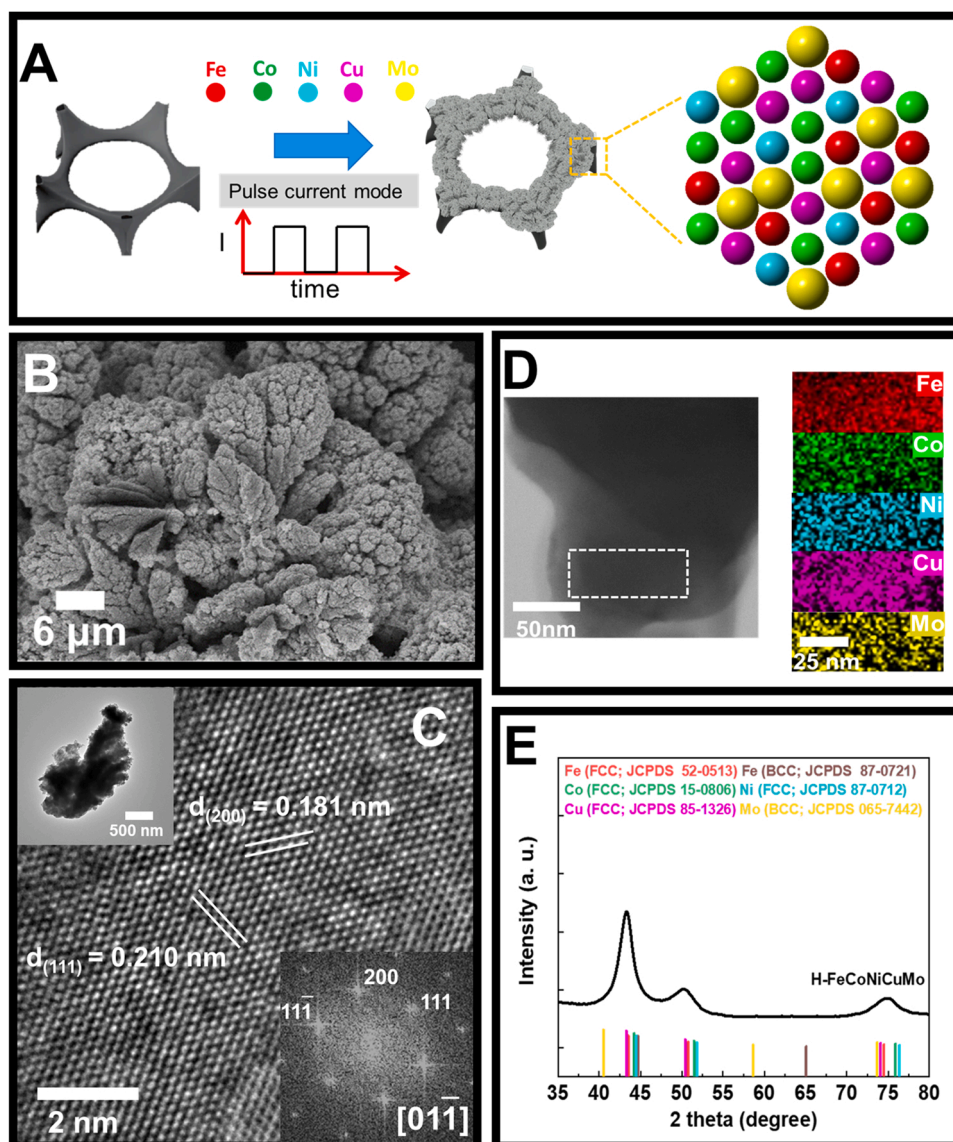
Fig. 1. (A) Schematic of fabrication process for H-FeCoNiCuMo. (B) SEM image of H-FeCoNiCuMo. (C) HRTEM image of FeCoNiCuMo HEA powder. (D) ABF-STEM image and EDX elemental mapping of FeCoNiCuMo HEA powder. (E) XRD pattern of HEA powders scratched off from corresponding HEA electrodes.

room temperature deposited HEAs normally is not satisfactory. The good crystallinity of the present HEAs may be attributed to the deposition conducted in a pulse current mode and at a moderate deposition temperature of 50 °C. To form a solid-solution HEA with an FCC lattice, it often requires: (1) small atomic size differences, $\delta \leq 8.5\%$, (2) suitable formation enthalpies (ΔH_{mix}, $-22 < \Delta H_{mix} < 7$ (kJ mol^{-1}), (3) suitable configurational entropies (ΔS_{config}), $11 \leq \Delta S_{config} \leq 19.5$ J (K·mol)$^{-1}$, and (4) large valence electron concentrations (VEC) ≥ 8 [26]. For the present FeCoNiCuMo HEA, $\delta = 3.57\%$, $\Delta H_{mix} = 3.68$ kJ mol^{-1}, $\Delta S_{config} = 13.3$ J K^{-1}mol^{-1}, and VEC = 8.85, further supporting its solid-solution FCC-phased HEA nature.

3.2. Evaluation of water splitting performances

Electrocatalytic performances of the HEA/MEA based electrodes are investigated in both 1 M KOH and 0.5 M H$_2$SO$_4$ for the HER and in 1 M KOH for the OER. These electrodes are not investigated in acidic media for the OER since the substrate of the electrode, nickel foam, cannot survive under the strong corrosive environment at applied anodic potentials, although H-FeCoNiCuMo shows good catalytic efficiency and reasonable stability in acidic OER when deposited on carbon papers

(Fig. S9) [28]. Figs. 2A, 2B, S8a, and S8b show the LSV curves of the sample electrodes and the Ni foam substrate, recorded at a scan rate of 1 mV s^{-1} in 1 M KOH, for the HER and OER. Overpotentials at specific current densities are determined from the LSV curves. Evidently, the contribution of the Ni foam substrate can be safely neglected. Both M-CoNiCuMo and H-FeCoNiCuMo achieve extraordinarily low overpotentials, single digit η_{10} and ≤ 100 mV η_{500} (6 and 7 mV for η_{10}, respectively; 90 and 100 mV for η_{500}, respectively), significantly outperforming M-FeCoNiCu ($\eta_{10} = 58$ mV; $\eta_{500} = 285$ mV), M-FeCoNiMo (38; 184), M-FeNiCuMo (21; 174), M-FeCoCuMo (20; 167), and Pt/C (15; 206, Fig. S10a), and competing favorably with top-ranked HER electrocatalysts reported in recent years (Fig. 2G; Table S12) [29–31]. It has been observed that Fe plays a relatively inert role in alloys for the HER in alkaline media because its presence is unfavorable for optimization of surface adsorption (H*)/desorption (H$_2$) energies [15]. In this regard, the presence of Fe in H-FeCoNiCuMo dilutes the strong synergistic effects between Co, Ni, Cu, and Mo, leading to slightly inferior performances of H-FeCoNiCuMo to M-CoNiCuMo. To further confirm the effect of Fe contents on alkaline HER, an Fe-rich H-FeCoNiCuMo electrode, with atomic ratios (at%) of Fe: Co: Ni: Cu: Mo being 32.5: 17.4: 15.7: 16.3: 18.1 (inset of Fig. S13), was fabricated and
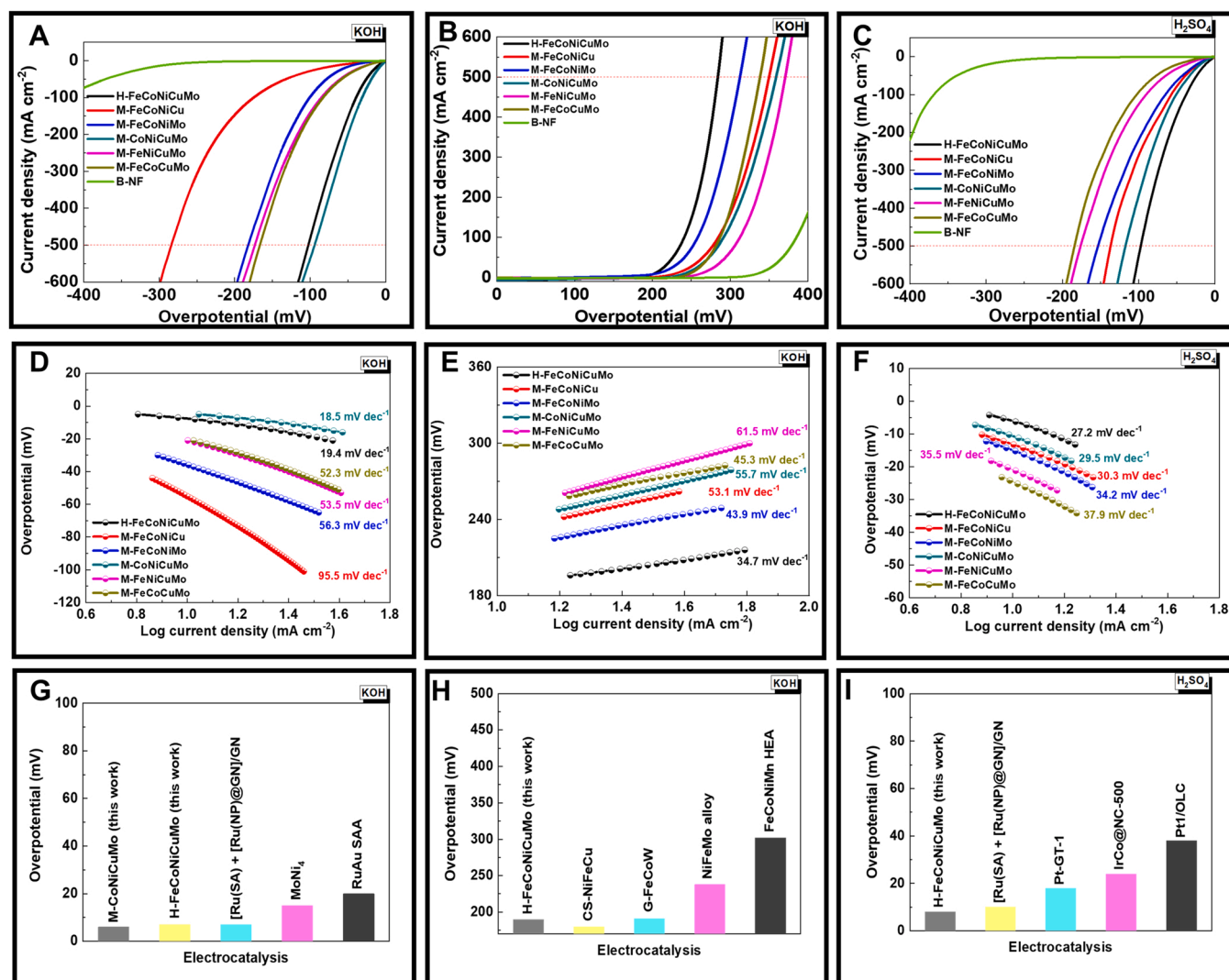
Fig. 2. Electrocatalytic water splitting performances of medium and high entropy alloys. (A) and (B) LSV curves for HER and OER in 1 M KOH. (C) LSV curves for HER in 0.5 M H_2SO_4. (D) Tafel plot for HER in 1 M KOH. (E) Tafel plot for OER in 1 M KOH. (F) Tafel plot for HER in 0.5 M H_2SO_4. (G), (H), and (I) Comparison of η_{10} for H-FeCoNiCuMo and/or M-CoNiCuMo with top-ranked HER and OER catalysts.

characterized. The LSV curve shows that the Fe-rich H-FeCoNiCuMo electrode exhibits HER performances inferior to those of the equi-molar H-FeCoNiCuMo electrode in 1 M KOH (Fig. S13: η_{10} = 21 mV; η_{500} = 155 mV), further confirming the relative inertness of Fe toward HER in alkaline media. On the other hand, it has been demonstrated that incorporation of Mo in Ni based alloy electrocatalysts greatly boosts the catalytic efficiency toward alkaline HER, through accelerating dissociation of H_2O, lowering the energy barrier of the electrochemical adsorption step, and accelerating the chemical desorption step all involved in the alkaline HER [30]. With this, M-FeCoNiCu, the only electrode without the presence of Mo, gives significantly higher η_{10} and η_{500} among the six electrodes.

Kinetic efficiency is next examined with Tafel slopes, which quantify the amount of potential increase needed to boost the current densities by ten-folds, and are determined in the current density range of 5–60 mA cm^{-2} (Fig. 2D). Both M-CoNiCuMo and H-FeCoNiCuMo exhibit extraordinarily low Tafel slopes less than 20 mV dec^{-1} (18.5 and 19.4 mV dec^{-1}, respectively), significantly outperforming M-FeCoNiCu (95.5 mV dec^{-1}), M-FeCoNiMo (56.4), M-FeNiCuMo (53.5), and M-FeCoCuMo (52.3). Electrochemical adsorption, electrochemical desorption, and chemical desorption, denoted as the Volmer, Heyrovsky, and Tafel steps, respectively, are the three fundamental reactions

well established for the HER. Theoretical Tafel slopes of 120, 40, and 30 mV dec^{-1} can be derived by treating the Volmer, Heyrovsky, and Tafel steps as the sole rate determining step (RDS), respectively [32,33]. The unusually low Tafel slopes achieved by H-FeCoNiCuMo and M-CoNiCuMo imply that more than one RDS may proceed simultaneously on different constituent elements of the alloy catalyst and positive synergistic effects between the two RDS's enhances the kinetic efficiency of the HER to achieve lower than 30 mV dec^{-1} Tafel slopes. Relevant experimental evidences and detailed discussions are presented in latter sections.

Catalytic efficiency of catalysts is a combined result of quality (average intrinsic activity) and quantity of exposed active sites of the catalyst [34]. For electrocatalysis, the average intrinsic activity and amount of the exposed active sites can be quantified as TOF and ECSA, respectively. TOF and ECSA are both overall manifestations of relevant factors, such as nanostructure, composition, defects, synergistic effects, catalyst layer thicknesses, electrode conductivity, interparticle resistances, etc. ECSA, linearly proportional to the double-layer capacitance (C_{dl}), can be determined from CV curves recorded at increasing scan rates within a non-Faradaic potential window (Figs. S11, S12, and Table S3). With ECSA available, TOF can be estimated from current densities achieved at a specific overpotential (Table S4 at −50 mV for

alkaline HER). H-FeCoNiCuMo possesses the highest ECSA ($117 cm^2_{ECSA}$).

slightly higher than that of M-CoNiCuMo (114 cm^2), but the second highest TOF (2.19 s^{-1}), appreciably lower than that of M-CoNiCuMo (2.94 s^{-1}), and the combined end result is the slightly higher catalytic efficiency of M-CoNiCuMo over H-FeCoNiCuMo. The presence of the relatively inert Fe in H-FeCoNiCuMo does dilute the strong synergistic effects arising from Co, Ni, Cu, and Mo, to reduce the TOF of H-FeCoNiCuMo to be appreciably lower than that of M-CoNiCuMo. In terms of TOF, H-FeCoNiCuMo and M-CoNiCuMo are significantly superior to top-ranked transition metal based alloy and precious metal based benchmark electrocatalysts, including, NiFeMo alloys (2.21 s^{-1} at −150 mV), and MoNi$_4$ alloys (0.4 s^{-1} at −50 mV) [30,35]. EIS is also conducted to study the charge transfer kinetics (manifested as R_{ct}) at the Faradaic processes. Here, EIS of the HER in 1 M KOH is conducted at $\eta = −165$ mV and the results are presented in Fig. S15 and Table S5. As expected, M-CoNiCuMo exhibits the smallest R_{ct}, appreciably less than that of H-FeCoNiCuMo and significantly lower than the other MEA electrodes, the same trend as that observed in TOF. In addition, the activation energies associated with H-FeCoNiCuMo and Pt/C toward alkaline HER were determined by first recording LSV curves at 298, 308, 318, 328, and 338 K in 1 M KOH (Fig. S14), followed by calculations based on the Arrhenius equation [36]. The activation energies thus obtained at an overpotential of 50 mV are 12.6 and 26.9 kJ mol^{-1} for H-FeCoNiCuMo and Pt/C, respectively, further supporting the extraordinary HER activities of H-FeCoNiCuMo.

H-FeCoNiCuMo is not only an extraordinarily outstanding electrode for alkaline HER, but also an outstanding electrode for alkaline OER, achieving a less than 200 mV η_{10} of 194 mV and a less than 300 mV η_{500} of 284 mV, making it an outstanding bifunctional electrode for overall water splitting in alkaline media and outperforming all MEA electrodes, including M-FeCoNiCu (η_{10} = 232 mV; η_{500} = 350 mV), M-FeCoNiMo (205; 310), M-CoNiCuMo (240; 360), M-FeNiCuMo (254; 371 mV), and M-FeCoCuMo (245; 339) (Fig. 2B), benchmark precious metal based oxides, such as IrO$_2$ (294; 519 mV, Fig. S10b) and RuO$_2$ (232; 634 mV, Fig. S10c), and almost all top-ranked OER electrocatalysts (Fig. 2H, Table S12) [17,37–39]. The presence of Fe, although making H-FeCoNiCuMo slightly inferior to M-CoNiCuMo for alkaline HER, is essential for the outstanding performance of H-FeCoNiCuMo toward alkaline OER. For metal/alloy electrocatalysts, a pre-OER oxidation step is necessary to generate OER-active species to catalyze the OER. In-situ Raman spectroscopy is conducted to reveal the details of the pre-OER step (Fig. S16). A broad scattering band emerges in the Raman shift range of 375–780 cm^{-1} at 200 mV and intensifies at 300 mV during the OER process. It disappears upon termination of the applied potential and resurges when resuming the potential to 300 mV, indicating the potential-dependent feature of the active species formation. The broad characteristic band recorded at 300 mV is separated into two sub-bands and de-convoluted to reveal the constituent active species formed in-situ at the pre-OER step (Fig. S17). The first sub-band, located at 375–620 cm^{-1}, is composed of four constituent peaks, including FeOOH (577 cm^{-1}), CoOOH (508 cm^{-1}), NiOOH (476 and 560 cm^{-1}), and Cu^{III}O$_2^-$ (603 cm^{-1}), whereas the second sub-band, located at 650–780 cm^{-1}, is composed of two constituent peaks, including FeOOH (690 cm^{-1}) and MoO$_2$ (720 cm^{-1}) [40–42]. For OER in alkaline media, a well accepted mechanism is as follows. It is a consecutive oxidation process by the hydroxide ion on the active site [43], starting with formation of hydroxides ($M + OH^- \rightarrow M - OH^* + e^-$), further with formation of oxides ($M - OH^* + OH^- \rightarrow M - O^* + H_2O_{(l)} + e^-$) and (oxy)hydroxides ($M - O^* + OH^- \rightarrow M - OOH^* + e^-$), followed by generation of oxygen through electrochemical desorption ($M - OOH^* + OH^- \rightarrow M + O_{2(g)} + H_2O_{(l)} + e^-$). Evidently, to trigger OER, active intermediates, such as hydroxides ($M\text{-}OH^*$), oxides ($M\text{-}O^*$), and (oxy) hydroxides ($M\text{-}OOH^*$), form in a pre-OER oxidation step. The emergence of characteristic peaks of NiOOH, FeOOH, CoOOH, Cu^{III}O$_2^-$, and MoO$_2$ is

observed at increasing overpotentials, indicating all five metallic elements of H-FeCoNiCuMo participate in the catalyzation of the OER. Metal (oxy)hydroxides have been well-identified as the active species for the OER and it has also been demonstrated that MoO$_2$ is OER-active [44]. Among the one HEA and five MEA electrodes, M-FeCoNiMo exhibits also outstanding OER performances in terms of overpotentials, with η_{10} and η_{500} only slightly inferior to those of H-FeCoNiCuMo but appreciably superior to the rest of the MEA electrodes. It implies that Cu is the relatively inert element toward alkaline OER among the five metal elements. Furthermore, an OER volcano plot for metal oxides, constructed by Seh et al. [45], shows that NiFe oxides and NiCo oxides are located on different wings of the volcano curve. This implies that relevant adsorption free energies of the OER descriptor may be optimized through suitable incorporation of Ni, Co, and Fe to realize enhanced OER activities. In addition to the highest catalytic efficiency, H-FeCoNiCuMo also possesses the highest kinetic efficiency, average intrinsic activity, and charge transfer efficiency as revealed by the smallest Tafel slope of 34.7 mV dec^{-1}, highest TOF of 5.85 (at 300 mV), and smallest R_{ct} of 0.119 Ω among all tested electrodes (Fig. 2E, Table S4, Fig. S18, and Table S6). In addition, H-FeCoNiCuMo shows an activation energy of 24.3 kJ mol^{-1}, obtained at an applied potential of 1.5 V in 1 M KOH, for alkaline OER, significantly lower than 44.1 kJ mol^{-1} achieved by the benchmark IrO$_2$ electrode (Figs. S14d-S14f), further supporting the outstanding OER activities of H-FeCoNiCuMo in alkaline media.

High entropy-stabilized solid solution alloys are endued excellent corrosion resistances through minimizing structural defects, that are vulnerable to corrosive attacks, with locally-disordered chemical environment [46]. Here, electrocatalytic performances of H-FeCoNiCuMo toward the HER in highly corrosive media, 0.5 M H$_2$SO$_4$ are also evaluated. H-FeCoNiCuMo again exhibits extraordinarily outstanding catalytic efficiency with a single digit η_{10} of 9 mV and close to 100 mV η_{500} of 104 mV, outperforming all MEA electrodes, including M-FeCoNiCu (η_{10} = 15 mV; η_{500} = 160 mV), M-FeCoNiMo (17; 168), M-CoNiCuMo (13; 121), M-FeNiCuMo (28; 174), and M-FeCoCuMo (34; 182), benchmark precious metal based Pt/C (14; 136, Fig. S19), and top-ranked HER electrocatalysts (Fig. 2C, S8c, and 2I, Table S13) [47–50]. In contrast to alkaline HER, Fe is no longer a relatively inert element in H-FeCoNiCuMo in acidic HER, although M-CoNiCuMo still appears to be the second most efficient catalyst. Additionally, Mo is no longer the strong promoter since M-FeCoNiCu, the only MEA electrode without the presence of Mo, competes comparably with other MEA electrodes in acidic HER. H-FeCoNiCuMo also possesses the highest electrochemically active surface area, kinetic efficiency, average intrinsic activity, and charge transfer efficiency as revealed by the highest C_{dl} of 11.8 mF cm^{-2}, smallest Tafel slope of 27.2 mV dec^{-1}, highest TOF of 0.87 (at −50 mV), and smallest R_{ct} of 0.026 Ω among all tested electrodes (Fig. 2F, Figs. S20-S22, Table S7, and Table S8). All tested HEA and MEA electrodes exhibit Tafel slopes ranging from 27.2 to 37.9 mV dec^{-1}, suggesting that the acidic HER proceeds through the Volmer-Tafel route with the Tafel reaction as the rate-determining step [32]. In addition, H-FeCoNiCuMo shows an activation energy of 25.9 kJ mol^{-1}, obtained at an overpotential of 50 mV in 0.5 M H$_2$SO$_4$, for acidic HER, slightly lower than 27.2 kJ mol^{-1} achieved by the benchmark Pt/C electrode (Fig. S23), further supporting the outstanding HER activities of H-FeCoNiCuMo in acidic media.

H-FeCoNiCuMo is in fact an outstanding pH-universal electrode. It also delivers outstanding electrocatalytic performances in neutral media. Here, we take 1 M PBS solutions as one example. H-FeCoNiCuMo gives η_{10} and η_{500} of 18 and 310 mV (Fig. S24), respectively for the HER and 210 and 632 mV (Fig. S25), respectively for the OER, outperforming those achieved by top-ranked neutral water splitting electrocatalysts, including η_{10} of 48 mV for CrO$_x$/Cu-Ni for the HER and η_{10} of 293 mV for karst NF for the OER in neutral media [51,52].

Nickel foams are a popular substrate for accommodation of active materials for electrocatalytic reactions. They possess many advantageous characteristics, including large surface areas for effective

accommodation and dispersion of active materials, three-dimensionally connected pathways for fast charge transport, and large pores for easy mass transport of electrolytes. H-FeCoNiCuMo however is intrinsically electrocatalytically active and performs outstandingly even when deposited on planar substrates, for example nickel plates (NP). Fig. S26 shows the outstanding alkaline HER and OER performances of H-FeCoNiCuMo/NP, only slightly inferior to those of H-FeCoNiCuMo/NF.

3.3. In-situ X-Ray absorption spectroscopy study

In-situ XAS technique is conducted to investigate the reaction mechanism of H-FeCoNiCuMo toward the HER. X-ray absorption near edge structure (XANES) spectra, together with the first derivatives of XANES spectra, recorded for H-FeCoNiCuMo and relevant metal/metallic compound standards at increasing reduction potentials, confirm that all constituent elements remain metallic during the HER,

implying that metallic elements are themselves the active species for the HER in both alkaline and acidic media (1 M KOH and 0.5 M H_2SO_4) (Figs. S27-S31). Evidently, the five constituent elements of H-FeCoNiCuMo catalyze the HER without being converted to compounds of higher/lower oxidation states. Note that adsorption of hydrogen atoms onto the active sites does not change the oxidation states of the active sites. The same conclusion applies to M-FeCoNiCu (sample in the absence of Mo) and M-CoNiCuMo (sample in the absence of Fe) (Figs. S32-S39).

Phase-corrected FT-EXAFS spectra were obtained to gain further insights on reaction mechanisms (Fig. 3A-3E for H-FeCoNiCuMo, Figs. S40 and S41 for M-FeCoNiCu and M-CoNiCuMo, respectively). First, it can be concluded from the in-situ FT-EXAFS spectra (Fig. 3A-Fig. 3E) that all five constituent elements of H-FeCoNiCuMo are not in the state of single atoms, but in the state of a high entropy alloy, with all five constituent elements being randomly distributed in an FCC
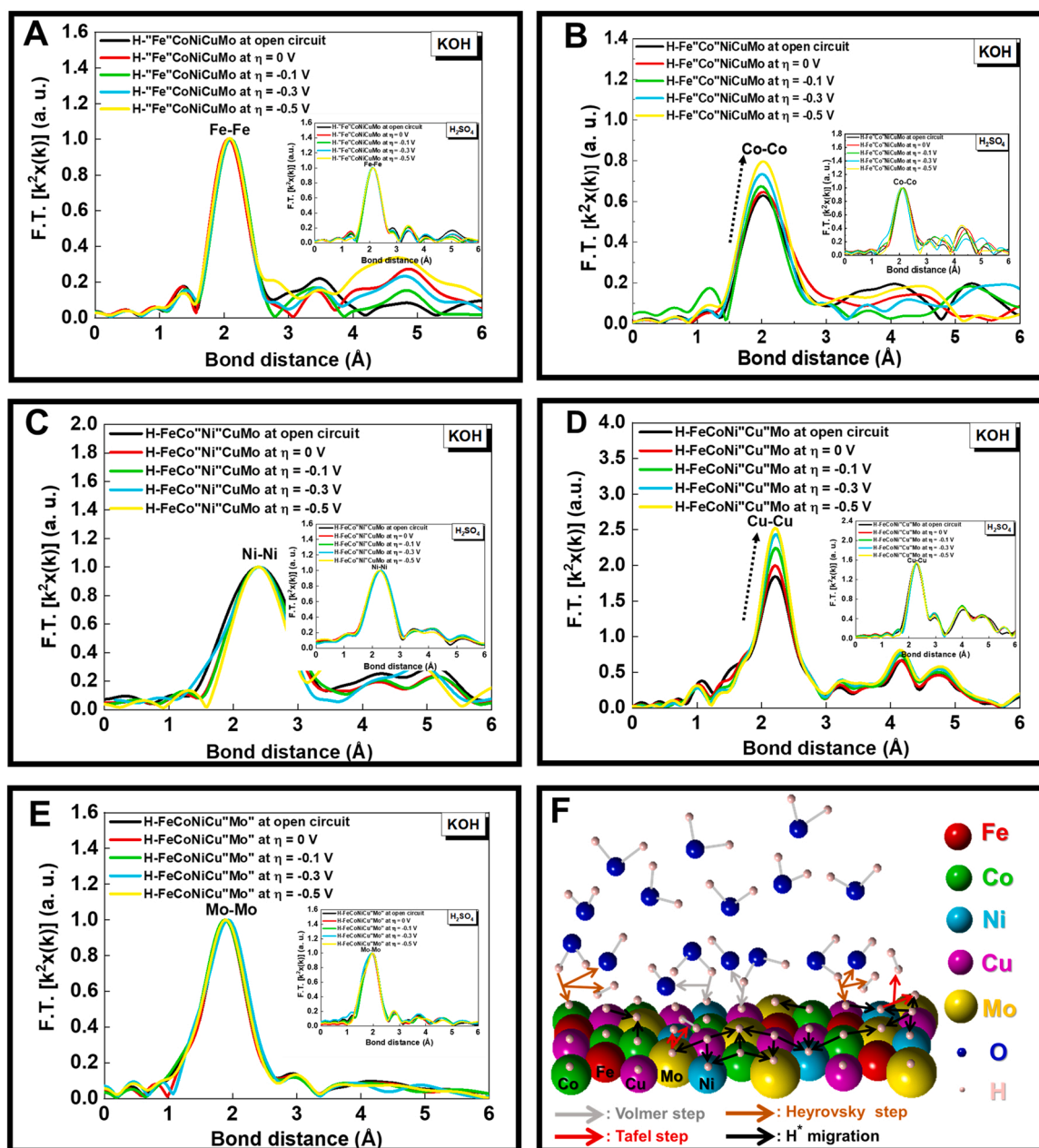

Fig. 3. (A) Fe, (B) Co, (C) Ni, (D) Cu, and (E) Mo FT-EXAFS spectra of H-FeCoNiCuMo recorded at increasing reduction potentials in 1 M KOH and 0.5 M H_2SO_4 (insets). (F) Synergistic interactions between Volmer-Heyrovsky and Volmer-Tafel routes on HEA surface in alkaline medium.

crystalline structure, and remain so during the HER. For Fe, Ni, and Mo, the oscillation frequencies and amplitudes of the corresponding FT-XANES spectra remain the same at increasing reduction potentials, indicating that the atomic configurations of these three elements remain the same during the HER in both alkaline and acidic media. Remarkably, the oscillation amplitudes of the corresponding FT-XANES spectra of Co and Cu increase with increasing reduction potentials in 1 M KOH but remain unchanged in 0.5 M H_2SO_4. The increase in oscillation amplitude signifies enhancement in coordination extent of the atom, implying that Co and Cu experience slow and intensive coordination with surrounding species during the RDS of the HER in alkaline media (1 M KOH). This slow and intensive coordination however does not occur for Co and Cu in acidic media (0.5 M H_2SO_4) and for Fe, Ni, and Mo in both alkaline and acidic media. This oscillation amplitude enhancement phenomenon disappears when the reduction potential is turned off for 10 min but resurges upon resuming the reduction potential (Fig. S42). In alkaline media, Volmer step proceeds as an electrochemical adsorption reaction ($H_2O + M + e^- \rightarrow OH^- + M\text{-}H^*$), followed by generation of H_2 through an electrochemical desorption (Heyrovsky step: $M\text{-}H^* + H_2O + e^- \rightarrow H_2 + OH^- + M$) or a chemical desorption (Tafel step: $M\text{-}H^* + M\text{-}H^* \rightarrow H_2 + 2$ M) step [32]. Summing up the above observation on FT-EXAFS spectra and the three fundamental steps, one can conclude that Co and Cu go through the rate-determining Heyrovsky step to generate H_2, in which $M\text{-}H^*$ proceeds with slow and intensive coordination with H_2O to cleave the H-O bond of H-O-H for subsequent release of H^* from $M\text{-}H^*$. The strong coordination of $M\text{-}H^*$ with H_2O is implied by the corresponding increase in oscillation amplitudes observed on the FT-EXAFS spectra during the HER at increasing reduction potentials. Consequently, Co and Cu catalyze the HER via the Volmer-Heyrovsky route in alkaline media but Volmer-Tafel route in acidic media. Furthermore, in alkaline media, both Volmer-Heyrovsky and Volmer-Tafel routes function simultaneously on different constituent elements of H-FeCoNiCuMo, whereas only the Volmer-Tafel route functions for the HER of H-FeCoNiCuMo in acidic media.

It has been pointed out that Ni and Mo possess intensive positive synergetic effects to efficiently drive the HER through the Volmer-Tafel route in alkaline media [13,30]. Besides, DFT simulations show that CoCu alloys exhibit low free energies of hydrogen adsorption for efficient HER [53]. The above two findings, together with the observation that Fe plays a relatively inert role in alkaline HER [15], suggest that the catalyzation of HER with H-FeCoNiCuMo in alkaline media can be discussed based on the categorical NiMo and CoCu pairs. The categorical NiMo pair, denoted as domain D_T, proceeds with the Volmer-Tafel route and the categorical CoCu pair, denoted as domain D_H, proceeds with the Volmer-Heyrovsky route. For both routes, the Volmer step (Fig. 3 F; gray arrow), giving formation of $M\text{-}H^*$ by breaking the H-O bond of H-O-H, proceeds fast to reach equilibria. On D_H, $M\text{-}H^*$ goes through the Heyrovsky step (Fig. 3 F; brown arrow) by breaking the H-O bond of H-O-H for H_2 generation, whereas on D_T, $M\text{-}H^*$ follows the Tafel step (Fig. 3 F; red arrow) to release H_2 through chemical desorption [22]. The synergistic interactions between the D_T and D_H domains make possible the lower than 30 mV dec^{-1} Tafel slopes achieved by H-FeCoNiCuMo (19.4 mV dec^{-1}) and M-CoNiCuMo (18.5 mV dec^{-1}) toward alkaline HER. It is also this synergistic interaction enables H-FeCoNiCuMo and M-CoNiCuMo to perform better in alkaline media than in acidic media in terms of overpotentials and Tafel slopes. A kinetic mode is proposed, postulating synergistic interactions between the D_T and D_H domains through migration of hydrogen adatoms (H^*) from D_H to D_T (Fig. 3 F; black arrow), to explain the ultralow Tafel slopes achieved by H-FeCoNiCuMo and M-CoNiCuMo. As detailed in Supporting Note of Supplementary Information, the interaction between D_H and D_T through hydrogen adatom migration can achieve Tafel slopes smaller than 30 mV dec^{-1}, the theoretical lower limit for the Volmer-Tafel route functioning on a single component catalyst. Through constructive synergy between constituent components of a multi-component catalyst, the lower limit for Tafel slopes can be further pushed down to 15 mV

dec^{-1}. Synergistic interactions between Volmer and Tafel steps proceeding on different domains of a catalyst have been reported to enhance the electrocatalytic performances of Ir nanoparticles decorated Si nanowires toward the HER in acidic media, achieving a lower than 30 mV dec^{-1} Tafel slope of 20 mV dec^{-1} [54]. The present work pushes the interaction scale down to well-mixed atomic configurations. The synergistic interaction between the D_T and D_H domains are particularly strong for HEA and even MEA catalysts because of the minimized interacting distances between atomically well-mixed constituent elements. This effect would diminish rapidly with increasing spatial distances between interacting species through formation of separated phases or nanograins.

The merit of HEA in elevating the synergistic effect between constituent elements is demonstrated by comparing the catalytic efficiency of H-FeCoNiCuMo with those of physically mixed Fe, Co, Ni, Cu, and Mo powders (Mix-FeCoNiCuMo) and mechanically alloyed phase separated FeCoNiCuMo catalysts (MA-FeCoNiCuMo) (Figs. S43-S45, XRD patterns in Fig. S46). Evidently, H-FeCoNiCuMo largely outperforms Mix-FeCoNiCuMo and MA-FeCoNiCuMo. The elemental compositions of the three electrodes are the same, but the interacting distances between constituent elements are orders of magnitude different.

3.4. Evaluation of H-FeCoNiCuMo catalysts in commercial environment

For industrial applications, alkaline electrolyzers should deliver high current densities at low cell voltages to achieve reduction in operation cost and to prolong life of electrocatalysts. H-FeCoNiCuMo works outstandingly for both HER and OER in alkaline media and serves as an outstanding bifunctional catalyst for alkaline overall water splitting. The H-FeCoNiCuMo//H-FeCoNiCuMo couple requires only ultralow cell voltages of 1.416 and 1.623 V to deliver current densities of 10 and 500 mA cm^{-2}, respectively, surpassing all MEA couples (M-FeCoNiCu: 1.523 and 1.881 V for 10 and 500 mA cm^{-2}, respectively; M-FeCoNiMo: 1.473 and 1.725 V; M-CoNiCuMo: 1.471 and 1.697 V; M-FeNiCuMo: 1.495 and 1.784 V; M-FeCoCuMo: 1.491 and 1.758 V) and all top ranked bifunctional electrocatalysts (Fig. 4 A, S47, and 4 C and Table S12) [26, 34,37,42,55–59]. Its kinetic efficiency is outstanding with an extraordinarily low, less than 100 mV dec^{-1} Tafel slope of 68.9 mV dec^{-1}, much lower than those achieved by the MEA couples (Fig. 4B).

For benchmarking against precious metal based electrocatalysts, H-FeCoNiCuMo exhibits significantly much better performances than IrO_2 and RuO_2 for the OER and Pt/C for the HER. The η_{10} and η_{500} achieved by Pt/C for the HER in 1 M KOH are 15 and 206 mV (vs. 7 and 100 mV for H-FeCoNiCuMo) (Fig. S10a), respectively, and are 14 and 136 mV in 0.5 M H_2SO_4, respectively (vs. 9 and 104 mV for H-FeCoNiCuMo) (Fig. S19). The η_{10} and η_{500} achieved by IrO_2 (RuO_2) for the OER in 1 M KOH are 294 and 519 mV (232 and 634 mV), respectively (vs. 189 and 281 mV for H-FeCoNiCuMo) (Figs. S10b and S10c). As for overall water splitting, the H-FeCoNiCuMo//H-FeCoNiCuMo couple outperforms the Pt/C//IrO_2 couple (Pt/C//RuO_2 couple) with cell voltages of 1.416 vs. 1.542 V (1.472 V) at 10 mA cm^{-2} and 1.623 vs. 1.964 V (2.027 V) at 500 mA cm^{-2} (Fig. S48).

Most importantly, the H-FeCoNiCuMo//H-FeCoNiCuMo couple exhibits ultrastability in harsh working environment, with a chronoamperometric (i-t) decay of only 2% and 1.5% after 100 hr continuous operations at a high initial current density of 500 mA cm^{-2} for overall water splitting in 1 M KOH and HER in 0.5 M H_2SO_4, respectively (Fig. 4D-4E). Here, make-up DI water was added per 24 h to maintain the pH value of the electrolyte. The ultrastability can be further confirmed with morphology (SEM images), electrocatalytic efficiency (LSV curves), surface oxidation states (HRXPS spectra), crystalline structure (XRD patterns), and composition (ICP-OES) of the catalysts before and after the stability tests for alkaline overall water splitting and acidic HER (Figs. S49-S61, Tables S9-S11). First, H-FeCoNiCuMo maintains its morphologies, electrochemical activities, oxidation states, and FCC phases after the long term HER stability tests in 1 M KOH and
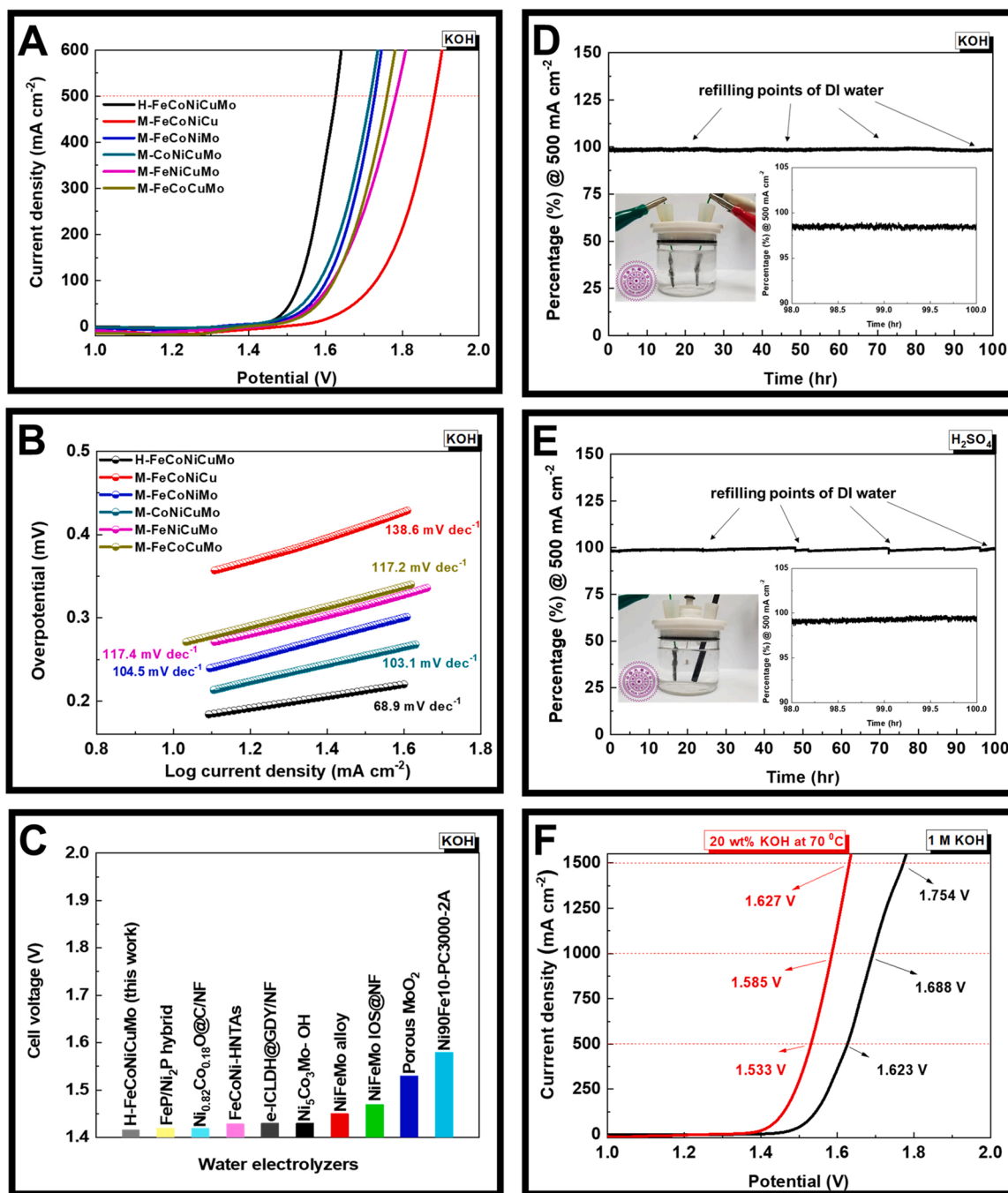
Fig. 4. Overall water splitting performances of MEAs and HEA. (A) LSV curves in 1 M KOH. (B) Tafel slopes in 1 M KOH. (C) Comparison of required cell voltages to achieve 10 mA cm^{-2} for H-FeCoNiCuMo with top-ranked precious-metal free bifunctional catalysts. (D) Chronoamperometric stability test of H-FeCoNiCuMo//H-FeCoNiCuMo couple for 100 hr operation at initial current density of 500 mA cm^{-2} in 1 M KOH. (E) Chronoamperometric stability test of H-FeCoNiCuMo for 100 hr HER operation at initial current density of 500 mA cm^{-2} in 0.5 M H$_2$SO$_4$. (F) LSV curves for overall water splitting of H-FeCoNiCuMo//H-FeCoNiCuMo couple in 1 M KOH at room temperature and in 20 wt% KOH at 70 °C.

0.5 M H$_2$SO$_4$. (Figs. S49, S51, S53, S54, S55, S56, and S58). As to H-FeCoNiCuMo after the long term alkaline OER stability test, significant Cu leaching occurred, as evident from the sample compositions determined with ICP-OES (Table S10). The Cu leaching led to a more porous structure of H-FeCoNiCuMo as shown in the SEM images of Fig. S50. Cu leaching however did not cause appreciable decay in OER activities of H-FeCoNiCuMo since Cu is relatively inert toward alkaline OER as discussed previously for Fig. 2B. This point can be further supported by the close matching of the LSV curves recorded before and after the long term OER stability test in 1 M KOH (Fig. S52). In addition, Fig. S60 shows

similar XRD patterns for H-FeCoNiCuMo before and after the OER stability test, indicating well maintained FCC phases. The surface oxidation states of H-FeCoNiCuMo before and after the stability test were next examined with HRXPS (Fig. S55 for before test, Fig. S56 for after alkaline HER test, Fig. S57 for after alkaline OER test, Fig. S58 for after acidic HER test). Evidently, the surface oxidation states of H-FeCoNiCuMo remain almost unchanged after the HER stability tests (comparison of Figs. S55, S56, and S58). As for the OER stability test, significant amounts of metal oxides, metal hydroxides, and metal (oxy)hydroxides emerge after the test (Fig. S57), including FeOOH (Fe2p$_{3/2}$; 712.5 eV),

FeO ($Fe2p_{3/2}$; 710.5 eV), CoO ($Co2p_{3/2}$; 780.2 eV), $Co(OH)_2$ ($Co2p_{3/2}$; 781.4 eV), CoOOH ($Co2p_{3/2}$; 780 eV), NiO ($Cu2p_{3/2}$;), ($Ni2p3/2$; 853.9 eV), $Ni(OH)_2$ ($Ni2p_{3/2}$; 855 eV), NiOOH ($Ni2p_{3/2}$; 856.1 eV), Cu_2O ($Cu2p_{3/2}$; 932.3 eV), CuO ($Cu2p_{3/2}$; 933.5 eV), $Cu(OH)_2$ ($Cu2p_{3/2}$; 935 eV), and MoO_2 (233.2 eV at $Mo3d_{3/2}$; 230 eV at $Mo3d_{5/2}$) [27,60, 61]. These compounds are the intermediate active species generated on the surface of H-FeCoNiCuMo during the pre-OER oxidation step for catalyzation of the subsequent OER [27,60,61]. Note that only Cu^+ and Cu^{2+} species are observed in the HRXPS spectra (Fig. S57d) for Cu. The more active $Cu^{III}O_2^-$ is only stable and detectable with in-situ techniques under high applied OER potentials [62].

The H-FeCoNiCuMo//H-FeCoNiCuMo couple is further examined for its electrocatalytic efficiency and stability in even harsher working environment commonly adopted for commercial electrolyzer operations, a high concentration of KOH of 20 wt%, ultrahigh current densities up to 1500 mA cm^{-2}, and a high temperature of 70 °C, in which higher electrocatalytic efficiency and much severer stability tests are expected [63]. The cell voltages required to deliver current densities of 500, 1000, 1500 mA cm^{-2} are only 1.533, 1.585, and 1.627 V, respectively, much lower than 1.623, 1.688, and 1.754 V, respectively achieved in 1 M KOH at room temperature (Fig. 4 F). The stability of the H-FeCoNiCuMo//H-FeCoNiCuMo couple, even under the extremely corrosive environment, operated in 20 wt% KOH at an initial current density of 1500 mA cm^{-2} at 70 °C for 100 h, remains outstanding, exhibiting a low chronoamperometric decay of 9% (Fig. S62). For comparison, a highly efficient and stable bifunctional metal organic framework (MOF) based electrocatalyst developed by our laboratory is also tested under the same condition. The electrode is composed of uniformly well-mixed Fe- and Ni-MOFs in-situ grown on skeleton surfaces of nickel foam (NF), termed as MFN-MOF/NF [64]. The MFN-MOF/NF//MFN-MOF/NF couple requires a low cell voltage of 1.80 V to achieve 500 mA cm^{-2} and experiences a chronopotentiometric decay of only 3.7% for operations at an initial current density of 500 mA cm^{-2} in 1 M KOH for 100 h. When operated in 20 wt% KOH at an initial current density of 1500 mA cm^{-2} at 70 °C, unlike the H-FeCoNiCuMo//H-FeCoNiCuMo couple, the MFN-MOF/NF//MFN -MOF/NF and also Pt/C//IrO$_2$ couples decay rapidly and substantially in short times (Fig. S62, Table S14).

The Faradaic efficiency of the H-FeCoNiCuMo//H-FeCoNiCuMo couple for the overall water splitting in 1 M KOH and of H-FeCoNiCuMo for the HER in 0.5 M H_2SO_4 are further estimated to confirm the absence of side reactions. A gas chromatography analyzer is used to measure the production rates of H_2 and O_2 for a continuous operation of the sample at an initial current density of 50 mA cm^{-2} for 60 min. The results agree well with corresponding theoretical values calculated from the measured current densities (Figs. S63-S64). Furthermore, the H_2/O_2 ratios are in excellent agreement with the theoretical value of 2, suggesting close to 100% Faradaic efficiency and thus absence of side reactions. Lastly, a video is offered to demonstrate the approach of coupled power-to-gas and gas-to-power for energy storage toward net-zero CO_2 emission. In the video, an electrolyzer, using H-FeCoNiCuMo as the anode and cathode, is driven with the electricity generated from a solar panel, illuminated with a solar simulator of one sun, to produce high purity hydrogen, which is fed into a fuel cell to provide electric power for an electrical fan (Movie S1) [45].

Supplementary material related to this article can be found online at doi:10.1016/j.apcatb.2022.122016.

4. Conclusion

In this study, we show that precious-metal-free high entropy alloys, composed of equi-molar Fe, Co, Ni, Cu, Mo (H-FeCoNiCuMo), are a breakthrough electrocatalyst for water splitting. H-FeCoNiCuMo, with high entropy-driven maximization of synergistic effects between catalyst constituents over atomic scales, exhibits extraordinary electrocatalytic efficiency and stability, giving single-digit overpotentials at 10 mA cm^{-2}, η_{10}, for hydrogen evolution reaction in both acidic (9 mV) and alkaline (7 mV) media, less than 200 mV η_{10} for oxygen evolution reaction in alkaline media (189 mV). In-situ X-Ray absorption study reveals a new catalytic phenomenon, two different catalytic mechanisms functioning simultaneously on different constituents of the catalyst, the Volmer-Heyrovsky route on Co and Cu and the Volmer-Tafel route on Ni and Mo. The present work demonstrates a new approach for design of breakthrough catalysts via engineering the strong synergistic effects between atomically/molecularly well-mixed constituents of multi-component catalysts over atomic/molecular scales.

Author contributions

C. L. H. conceived the idea and designed the experiments. C. L. H., S. Q. C., and Y. X. Y. carried out the synthesis, characterizations, and performance evaluation of the electrocatalysts, prepared figures, and co-wrote the manuscript. Y. G. L., C. L. C., C. K. P., and C. L. H. conducted high energy XRD and in-situ XAS measurements, and analyzed the data. C. L. H., C. T. H., and Y. A. C. performed detailed microscopic characterizations of the electrocatalysts. C. L. H., C. L. C., D. S. R., and S. Y. L. developed the HER mechanism in alkaline media. S. Y. L. directed the research, procured funds, and prepared the manuscript.

CRediT authorship contribution statement

Chun-Lung Huang: Conceptualization, Methodology, Formal analysis, Investigation, Writing – original draft. **Yan-Gu Lin:** Software, Formal analysis, Investigation. **Chao-Lung Chiang:** Software, Formal analysis, Investigation. **Chun-Kuo Peng:** Software, Formal analysis, Investigation. **Duraisamy Senthil Raja:** Investigation, Formal analysis. **Cheng-Ting Hsieh:** Investigation, Formal analysis. **Yu-An Chen:** Investigation, Formal analysis. **Shun-Qin Chang:** Investigation, Formal analysis. **Yong-Xian Yeh:** Investigation. **Shih-Yuan Lu:** Supervision, Conceptualization, Formal analysis, Funding acquisition, Investigation, Methodology, Project administration, Resources, Writing - review & editing.

Declaration of Competing Interest

The authors declare the following financial interests/personal relationships which may be considered as potential competing interests: The authors declare that National Tsing Hua University, Taiwan has filed patent applications (US 16819149, CN 202010021308. X, and TW 109100708) for the catalysts and their preparation method reported in the manuscript.

Data Availability

Data will be made available on request.

Acknowledgements

Conflicts of interest

The authors declare that National Tsing Hua University, Taiwan has filed patent applications (US 16819149, CN 202010021308. X, and TW 109100708) for the catalysts and their preparation method reported in the manuscript.

Appendix A. Supporting information

Supplementary data associated with this article can be found in the online version at doi:10.1016/j.apcatb.2022.122016.

References

[1] IEA 2017, Energy Technology Perspectives 2017, IEA, Paris. www.iea.org/reports/energy-technology-perspectives-2017.

[2] J. Xu, G.F. Froment, Methane steam reforming, methanation and water-gas shift: I. Intrinsic kinetics, AIChE J. 35 (1989) 88–96.

[3] N. Jiang, B. You, M. Sheng, Y. Sun, Electrodeposited cobalt-phosphorous-derived films as competent bifunctional catalysts for overall water splitting, Angew. Chem. Int. Ed. 54 (2015) 6251–6254.

[4] L. Zhang, C. Chang, C.-W. Hsu, C.-W. Chang, S.-Y. Lu, Hollow nanocubes composed of well-dispersed mixed metal-rich phosphides in N-doped carbon as highly efficient and durable electrocatalysts for the oxygen evolution reaction at high current densities, J. Mater. Chem. A 5 (2017) 19656–19663.

[5] X.-F. Chuah, C.-T. Hsieh, C.-L. Huang, D. Senthil Raja, H.-W. Lin, S.-Y. Lu, In-situ grown, passivator-modulated anodization derived synergistically well-mixed Ni-Fe oxides from Ni foam as high-performance oxygen evolution reaction electrocatalyst, ACS Appl. Energy Mater. 2 (2019) 743–753.

[6] C.-T. Hsieh, X.-F. Chuah, C.-L. Huang, H.-W. Lin, Y.-A. Chen, S.-Y. Lu, NiFe/(Ni,Fe)3S2 core/shell nanowire arrays as outstanding catalysts for electrolytic water splitting at high current densities, Small Methods 3 (2019) 1900234.

[7] H.-W. Lin, D. Senthil Raja, X.-F. Chuah, C.-T. Hsieh, Y.-A. Chen, S.-Y. Lu, Bimetallic MOFs possessing hierarchical synergistic effects as high performance electrocatalysts for overall water splitting at high current densities, Appl. Catal. B Environ. 258 (2019), 118023.

[8] C.-N. Lv, L. Zhang, X.-H. Huang, Y.-X. Zhu, X. Zhang, J.-S. Hu, S.-Y. Lu, Double functionalization of N-doped carbon carved hollow nanocubes with mixed metal phosphides as efficient bifunctional catalysts for electrochemical overall water splitting, Nano Energy 65 (2019), 103995.

[9] D. Senthil Raja, C.-L. Huang, Y.-A. Chen, Y. Choi, S.-Y. Lu, Composition-balanced trimetallic MOFs as ultra-efficient electrocatalysts for oxygen evolution reaction at high current densities, Appl. Catal. B Environ. 279 (2020), 119375.

[10] H. Li, J. Lai, Z. Li, L. Wang, Multi-sites electrocatalysis in high-entropy alloys, Adv. Funct. Mater. 31 (2021) 2106715.

[11] H. Liu, H. Qin, J. Kang, L. Ma, G. Chen, Q. Huang, Z. Zhang, E. Liu, H. Lu, J. Li, N. Zhao, A freestanding nanoporous NiCoFeMoMn high-entropy alloy as an efficient electrocatalyst for rapid water splitting, Chem. Eng. J. 435 (2022), 134898.

[12] R. Li, X. Liu, W. Liu, Z. Li, K.C. Chan, Z. Lu, Design of hierarchical porosity via manipulating chemical and microstructural complexities in high-entropy alloys for efficient water electrolysis, Adv. Science 9 (2022) 2105808.

[13] Y.-Y. Chen, Y. Zhang, X. Zhang, T. Tang, H. Luo, S. Niu, Z.-H. Dai, L.-J. Wan, J.-S. Hu, Self-templated fabrication of MoNi4/MoO3-x nanorod arrays with dual active components for highly efficient hydrogen evolution, Adv. Mater. 29 (2017) 1703311.

[14] Y. Shen, Y. Zhou, D. Wang, X. Wu, J. Li, J. Xi, Nickel-copper alloy encapsulated in graphitic carbon shells as electrocatalysts for hydrogen evolution reaction, Adv. Energy Mater. 8 (2018) 1701759.

[15] C. Liang, P. Zou, A. Nairan, Y. Zhang, J. Liu, K. Liu, S. Hu, F. Kang, H.J. Fan, C. Yang, Exceptional performance of hierarchical Ni-Fe oxyhydroxide@NiFe alloy nanowire array electrocatalysts for large current density water splitting, Energy Environ. Sci. 13 (2020) 86–95.

[16] L. Yu, H. Zhou, J. Sun, F. Qin, F. Yu, J. Bao, Y. Yu, S. Chen, Z. Ren, Cu nanowires shelled with NiFe layered double hydroxide nanosheets as bifunctional electrocatalysts for overall water splitting, Energy Environ. Sci. 10 (2017) 1820–1827.

[17] B. Zhang, X. Zheng, O. Voznyy, R. Comin, M. Bajdich, M. García-Melchor, L. Han, J. Xu, M. Liu, L. Zheng, F.P. García de Arquer, T. Dinh Cao, F. Fan, M. Yuan, E. Yassitepe, N. Chen, T. Regier, P. Liu, Y. Li, P. De Luna, A. Janmohamed, L. Xin Huolin, H. Yang, A. Vojvodic, H. Sargent, Edward, Homogeneously dispersed multimetal oxygen-evolving catalysts, Science 352 (2016) 333–337.

[18] X. Han, N. Li, Y.B. Kang, Q. Dou, P. Xiong, Q. Liu, J.Y. Lee, L. Dai, H.S. Park, Unveiling trifunctional active sites of a heteronanosheet electrocatalyst for integrated cascade battery/electrolyzer systems, ACS Energy Lett. 6 (2021) 2460–2468.

[19] H. Yang, X. Han, A.I. Douka, L. Huang, L. Gong, C. Xia, H.S. Park, B.Y. Xia, Advanced oxygen electrocatalysis in energy conversion and storage, Adv. Funct. Mater. 31 (2021) 2007602.

[20] J.W. Yeh, S.K. Chen, S.J. Lin, J.Y. Gan, T.S. Chin, T.T. Shun, C.H. Tsau, S.Y. Chang, Nanostructured high-entropy alloys with multiple principal elements: novel alloy design concepts and outcomes, Adv. Eng. Mater. 6 (2004) 299–303.

[21] D.B. Miracle, O.N. Senkov, A critical review of high entropy alloys and related concepts, Acta Mater. 122 (2017) 448–511.

[22] K. Huang, B. Zhang, J. Wu, T. Zhang, D. Peng, X. Cao, Z. Zhang, Z. Li, Y. Huang, Exploring the impact of atomic lattice deformation on oxygen evolution reactions based on a sub-5 nm pure face-centred cubic high-entropy alloy electrocatalyst, J. Mater. Chem. A 8 (2020) 11938–11947.

[23] P. Ma, S. Zhang, M. Zhang, J. Gu, L. Zhang, Y. Sun, W. Ji, Z. Fu, Hydroxylated high-entropy alloy as highly efficient catalyst for electrochemical oxygen evolution reaction, Sci. China Mater. 63 (2020) 2613–2619.

[24] H. Li, Y. Han, H. Zhao, W. Qi, D. Zhang, Y. Yu, W. Cai, S. Li, J. Lai, B. Huang, L. Wang, Fast site-to-site electron transfer of high-entropy alloy nanocatalyst driving redox electrocatalysis, Nat. Commun. 11 (2020) 5437.

[25] T.A.A. Batchelor, J.K. Pedersen, S.H. Winther, I.E. Castelli, K.W. Jacobsen, J. Rossmeisl, High-entropy alloys as a discovery platform for electrocatalysis, Joule 3 (2019) 834–845.

[26] S. Guo, C.T. Liu, Phase stability in high entropy alloys: formation of solid-solution phase or amorphous phase, Prog. Nat. Sci. Mater. Int. 21 (2011) 433–446.

[27] C.-L. Huang, X.-F. Chuah, C.-T. Hsieh, S.-Y. Lu, NiFe alloy nanotube arrays as highly efficient bifunctional electrocatalysts for overall water splitting at high current densities, ACS Appl. Mater. Interfaces 11 (2019) 24096–24106.

[28] S.-Q. Chang, C.-C. Cheng, P.-Y. Cheng, C.-L. Huang, S.-Y. Lu, Pulse electrodeposited FeCoNiMnW high entropy alloys as efficient and stable bifunctional electrocatalysts for acidic water splitting, Chem. Eng. J. 446 (2022), 137452.

[29] J.N. Tiwari, A.M. Harzandi, M. Ha, S. Sultan, C.W. Myung, H.J. Park, D.Y. Kim, P. Thangavel, A.N. Singh, P. Sharma, S.S. Chandrasekaran, F. Salehnia, J.-W. Jang, H.S. Shin, Z. Lee, K.S. Kim, High-performance hydrogen evolution by ru single atoms and nitrided-Ru nanoparticles implanted on N-doped graphitic sheet, Adv. Energy Mater 9 (2019) 1900931.

[30] J. Zhang, T. Wang, P. Liu, Z. Liao, S. Liu, X. Zhuang, M. Chen, E. Zschech, X. Feng, Efficient hydrogen production on MoNi4 electrocatalysts with fast water dissociation kinetics, Nat. Commun 8 (2017) 15437.

[31] C.-H. Chen, D. Wu, Z. Li, R. Zhang, C.-G. Kuai, X.-R. Zhao, C.-K. Dong, S.-Z. Qiao, H. Liu, X.-W. Du, Ruthenium-based single-atom alloy with high electrocatalytic activity for hydrogen evolution, Adv. Energy Mater. 9 (2019) 1803913.

[32] T. Shinagawa, A.T. Garcia-Esparza, K. Takanabe, Insight on Tafel slopes from a microkinetic analysis of aqueous electrocatalysis for energy conversion, Sci. Rep. 5 (2015) 13801.

[33] B. You, Y. Sun, Innovative strategies for electrocatalytic water splitting, Acc. Chem. Res. 51 (2018) 1571–1580.

[34] J. Kibsgaard, T.F. Jaramillo, Molybdenum phosphosulfide: an active, acid-stable, earth-abundant catalyst for the hydrogen evolution reaction, Angew. Chem. Int. Ed. 53 (2014) 14433–14437.

[35] C.-T. Hsieh, C.-L. Huang, Y.-A. Chen, S.-Y. Lu, NiFeMo alloy inverse-opals on Ni foam as outstanding bifunctional catalysts for electrolytic water splitting of ultralow cell voltages at high current densities, Appl. Catal. B Environ. 267 (2020), 118376.

[36] B. Yang, J. Xu, D. Bin, J. Wang, J. Zhao, Y. Liu, B. Li, X. Fang, Y. Liu, L. Qiao, L. Liu, B. Liu, Amorphous phosphatized ruthenium-iron bimetallic nanoclusters with Pt-like activity for hydrogen evolution reaction, Appl. Catal. B Environ. 283 (2021), 119583.

[37] P. Zhang, L. Li, D. Nordlund, H. Chen, L. Fan, B. Zhang, X. Sheng, Q. Daniel, L. Sun, Dendritic core-shell nickel-iron-copper metal/metal oxide electrode for efficient electrocatalytic water oxidation, Nat. Commun. 9 (2018) 381.

[38] F. Qin, Z. Zhao, M.K. Alam, Y. Ni, F. Robles-Hernandez, L. Yu, S. Chen, Z. Ren, Z. Wang, J. Bao, Trimetallic NiFeMo for overall electrochemical water splitting with a low cell voltage, ACS Energy Lett. 3 (2018) 546–554.

[39] W. Dai, T. Lu, Y. Pan, Novel and promising electrocatalyst for oxygen evolution reaction based on MnFeCoNi high entropy alloy, J. Power Sources 430 (2019) 104–111.

[40] Z. Qiu, C.-W. Tai, G.A. Niklasson, T. Edvinsson, Direct observation of active catalyst surface phases and the effect of dynamic self-optimization in NiFe-layered double hydroxides for alkaline water splitting, Energy Environ. Sci. 12 (2019) 572–581.

[41] R. Li, B. Hu, T. Yu, H. Chen, Y. Wang, S. Song, Insights into correlation among surface-structure-activity of cobalt-derived pre-catalyst for oxygen evolution reaction, Adv.Sci. 7 (2020) 1902830.

[42] Y. Deng, B.S. Yeo, Characterization of electrocatalytic water splitting and CO2 reduction reactions using in situ/operando raman spectroscopy, ACS Catal. 7 (2017) 7873–7889.

[43] J. Song, C. Wei, Z.-F. Huang, C. Liu, L. Zeng, X. Wang, Z.J. Xu, A review on fundamentals for designing oxygen evolution electrocatalysts, Chem. Soc. Rev. 49 (2020) 2196–2214.

[44] Y. Jin, H. Wang, J. Li, X. Yue, Y. Han, P.K. Shen, Y. Cui, Porous MoO2 nanosheets as non-noble bifunctional electrocatalysts for overall water splitting, Adv. Mater. 28 (2016) 3785–3790.

[45] W. Seh Zhi, J. Kibsgaard, F. Dickens Colin, I. Chorkendorff, K. Nørskov Jens, F. Jaramillo, Thomas, Combining theory and experiment in electrocatalysis: Insights into materials design, Science 355 (2017) eaad4998.

[46] Y. Shi, B. Yang, P.K. Liaw, Corrosion-resistant high-entropy alloys: a review, Metals 7 (2017).

[47] J.N. Tiwari, S. Sultan, C.W. Myung, T. Yoon, N. Li, M. Ha, A.M. Harzandi, H. J. Park, D.Y. Kim, S.S. Chandrasekaran, W.G. Lee, V. Vij, H. Kang, T.J. Shin, H. S. Shin, G. Lee, Z. Lee, K.S. Kim, Multicomponent electrocatalyst with ultralow Pt loading and high hydrogen evolution activity, Nat. Energy 3 (2018) 773–782.

[48] P. Jiang, J. Chen, C. Wang, K. Yang, S. Gong, S. Liu, Z. Lin, M. Li, G. Xia, Y. Yang, J. Su, Q. Chen, Tuning the activity of carbon for electrocatalytic hydrogen

evolution via an iridium-cobalt alloy core encapsulated in nitrogen-doped carbon cages, Adv. Mater. 30 (2018) 1705324.

[49] D. Liu, X. Li, S. Chen, H. Yan, C. Wang, C. Wu, Y.A. Haleem, S. Duan, J. Lu, B. Ge, P. M. Ajayan, Y. Luo, J. Jiang, L. Song, Atomically dispersed platinum supported on curved carbon supports for efficient electrocatalytic hydrogen evolution, Nat. Energy 4 (2019) 512–518.

[50] G. Zhang, K. Ming, J. Kang, Q. Huang, Z. Zhang, X. Zheng, X. Bi, High entropy alloy as a highly active and stable electrocatalyst for hydrogen evolution reaction, Electrochim. Acta 279 (2018) 19–23.

[51] C.-T. Dinh, A. Jain, F.P.G. de Arquer, P. De Luna, J. Li, N. Wang, X. Zheng, J. Cai, B. Z. Gregory, O. Voznyy, B. Zhang, M. Liu, D. Sinton, E.J. Crumlin, E.H. Sargent, Multi-site electrocatalysts for hydrogen evolution in neutral media by destabilization of water molecules, Nat. Energy 4 (2019) 107–114.

[52] X. Gao, Y. Chen, T. Sun, J. Huang, W. Zhang, Q. Wang, R. Cao, Karst landform-featured monolithic electrode for water electrolysis in neutral media, Energy Environ. Sci. 13 (2020) 174–182.

[53] J. Greeley, T.F. Jaramillo, J. Bonde, I. Chorkendorff, J.K. Nørskov, Computational high-throughput screening of electrocatalytic materials for hydrogen evolution, Nat. Mater. 5 (2006) 909–913.

[54] M. Sheng, B. Jiang, B. Wu, F. Liao, X. Fan, H. Lin, Y. Li, Y. Lifshitz, S.-T. Lee, M. Shao, Approaching the volcano top: iridium/silicon nanocomposites as efficient electrocatalysts for the hydrogen evolution reaction, ACS Nano 13 (2019) 2786–2794.

[55] F. Yu, H. Zhou, Y. Huang, J. Sun, F. Qin, J. Bao, W.A. Goddard, S. Chen, Z. Ren, High-performance bifunctional porous non-noble metal phosphide catalyst for overall water splitting, Nat. Commun. 9 (2018) 2551.

[56] H. Yang, Z. Chen, W. Hao, H. Xu, Y. Guo, R. Wu, Catalyzing overall water splitting at an ultralow cell voltage of 1.42 V via coupled Co-doped NiO nanosheets with carbon, Appl. Catal. B Environ. 252 (2019) 214–221.

[57] H. Li, S. Chen, Y. Zhang, Q. Zhang, X. Jia, Q. Zhang, L. Gu, X. Sun, L. Song, X. Wang, Systematic design of superaerophobic nanotube-array electrode comprised of transition-metal sulfides for overall water splitting, Nat. Commun. 9 (2018) 2452.

[58] L. Hui, Y. Xue, B. Huang, H. Yu, C. Zhang, D. Zhang, D. Jia, Y. Zhao, Y. Li, H. Liu, Y. Li, Overall water splitting by graphdiyne-exfoliated and -sandwiched layered double-hydroxide nanosheet arrays, Nat. Commun. 9 (2018) 5309.

[59] S. Hao, L. Chen, C. Yu, B. Yang, Z. Li, Y. Hou, L. Lei, X. Zhang, NiCoMo hydroxide nanosheet arrays synthesized via chloride corrosion for overall water splitting, ACS Energy Lett. 4 (2019) 952–959.

[60] P.A. Spevack, N.S. McIntyre, Thermal reduction of molybdenum trioxide, J. Phys. Chem. 96 (22) (1992) 9029–9035.

[61] S. Song, H. Bao, X. Lin, X.-L. Du, J. Zhou, L. Zhang, N. Chen, J. Hu, J.-Q. Wang, Molten salt-assisted synthesis of bulk CoOOH as a water oxidation catalyst, J. Energy Chem. 42 (2020) 5–10.

[62] C.-L. Huang, K. Sasaki, D. Senthil Raja, C.-T. Hsieh, Y.-J. Wu, J.-T. Su, C.-C. Cheng, P.-Y. Cheng, S.-H. Lin, Y. Choi, S.-Y. Lu, Twinning enhances efficiencies of metallic catalysts toward electrolytic water splitting, Adv. Energy Mater. 11 (46) (2021) 2101827.

[63] I. Vincent, D. Bessarabov, Low cost hydrogen production by anion exchange membrane electrolysis: a review, Renew. Sustain. Energy Rev. 81 (2018) 1690–1704.

[64] D. Senthil Raja, H.-W. Lin, S.-Y. Lu, Synergistically well-mixed MOFs grown on nickel foam as highly efficient durable bifunctional electrocatalysts for overall water splitting at high current densities, Nano Energy 57 (2019) 1–13.